Selective averaging for high-resolution solid-state NMR spectroscopy of aligned samples

Alexander A. Nevzorov, Stanley J. Opella [*]

Department of Chemistry and Biochemistry, University of California, San Diego, 9500 Gilman Drive, La Jolla, CA 92093-0307, USA

Abstract

Solid-state NMR experiments benefit from being performed at high fields, and this is essential in order to obtain spectra with the resolution and sensitivity required for applications to protein structure determination in aligned samples. Since the amount of rf power that can be applied is limited, especially for aqueous protein samples, the most important pulse sequences suffer from bandwidth limitations resulting from the same spread in chemical shift frequencies that aids resolution. SAMPI4 is a pulse sequence that addresses these limitations. It yields separated local field spectra with narrower and more uniform linewidths over the entire spectrum than the currently used PISEMA and SAMMY experiments. In addition, it is much easier to set up on commercial spectrometers and can be incorporated as a building block into other multidimensional pulse sequences. This is illustrated with a two-dimensional HETCOR experiment, where it is crucial to transfer polarization from the amide protons to their directly bonded nitrogens over a wide range of chemical shift frequencies. A quantum-mechanical treatment of the spin Hamiltonians under high-power rf pulses is presented which gives the scaling factor for SAMPI4 as well as the durations of the rf pulses to achieve optimal decoupling.
© 2006 Elsevier Inc. All rights reserved.

Keywords: Selective averaging; Average Hamiltonian theory; Separated local field spectroscopy; Homonuclear decoupling; SAMPI4; SAMMY; PISEMA

1. Introduction

It is now possible to obtain well-resolved spectra of proteins in biological supramolecular complexes, such as virus particles or membranes, by using the methods, instruments, and theories of high-resolution solid-state NMR spectroscopy. High magnetic fields are essential to obtain the requisite sensitivity and chemical shift resolution, however the resulting large spans of frequencies place these experiments at the edge of feasibility using currently available methods and instruments. In order to study larger and more complex proteins the bandwidth limitations of the experimental methods have to be dealt with. This requires consideration of the most fundamental aspects of the averaging of nuclear spin interactions by radiofrequency pulses. Since the

proteins in these complexes are immobile on the relevant NMR timescales (10^4 Hz), motional averaging through molecular reorientation cannot be invoked, and in the case of magic angle sample spinning, which can be extremely effective with polycrystalline solids, there is an unwanted averaging of the orientational parameters that are the source of structural information in solid-state NMR of aligned samples.

In solid-state NMR spectroscopy it is essential to deal with many-body systems of strongly interacting spins. In most cases, these pair-wise interactions can be reduced to heteronuclear and homonuclear dipolar couplings. To obtain tractable high-resolution NMR spectra of such systems, it is necessary to manipulate these interactions in order to eliminate the homonuclear dipolar couplings, which would otherwise broaden the resonance linewidths due to spin diffusion. A variety of methods have been developed to eliminate or reduce the broadening effects of homonuclear dipolar couplings, including: magic-angle spinning

[*] Corresponding author. Fax: +1 858 822 4821.
E-mail address: sopella@ucsd.edu (S.J. Opella).

(MAS) [1–3], magic angle radiofrequency irradiation [4–6], multiple pulse-sequences that utilize discrete radiofrequency pulses such as WAHUHA [7], MREV [8], BR-24 [9], BLEW-12 [10], the recently developed HIMSELF sequences [11–13], T-MREV [14], Magic Sandwiches [15,16], and HOT [17] versions of BLEW-12 and Magic Sandwiches. In rotating solids, composite pulse sequences have been developed that compensate for offset effects and rf amplitude imperfections [18]. The theoretical basis for the design of such homonuclear pulse sequence is provided by average Hamiltonian theory (AHT) as pioneered by Waugh and co-workers [19,20].

The situation is more complicated for heteronuclear spin systems where in addition to the "abundant" I spins (i.e. ^1H), the properties of individual "dilute" S spins, e.g. ^{15}N or ^{13}C, are essential components of the system; this makes the network of interactions much more diverse, and the rigorous AHT methods quickly lead to unwieldy mathematical expressions. This is especially true for stationary solid samples, where the strong proton–proton interaction Hamiltonian does not commute with the others. It complicates the theoretical analysis and pulse-sequence design for the measurement of resolved heteronuclear dipolar couplings in the presence of homonuclear decoupling as in separated local field spectroscopy [21]. Another factor is that in solid-state NMR of stationary solid samples heteronuclear spin exchange is usually implemented through cross-polarization under Hartmann–Hahn matching conditions, which introduces an additional radiofrequency (rf) Hamiltonian for most of the evolution of the system. In order to further develop solid-state NMR spectroscopy of proteins, a framework is needed for treating the homonuclear and heteronuclear interactions in the presence of continuous radiofrequency pulses where the δ-pulse approximation is invalid.

In this Article, we describe an approach to treating the complex homo- and hetero-nuclear spin systems found in proteins using simple symmetry principles and the truncated Hamiltonian approximation under the assumption of high-power rf pulses. As a practical matter, this approach enabled us to rationalize and improve the pulse sequence, SAMMY [22], which is complementary to PISEMA [23], as a method for obtaining high resolution separated local field spectra of proteins. In addition, this method of treating the interaction Hamiltonians under high-power (but finite) pulses has the potential to be useful in developing new pulse sequences for strongly coupled spin systems.

Solid-state NMR of proteins is a burgeoning area of research; membrane proteins are of particular interest, since they comprise about 30% of the human genome, and their structure determination poses substantial challenges to the standard X-ray crystallography and solution NMR methods. Solid-state NMR of aligned samples is particularly well suited for membrane proteins in lipid bilayers, since the immobilization and alignment of the protein are naturally imposed by the membrane environment itself. In this approach, the protein structure is calculated from the constraints resulting from the orientation-dependent NMR observables (e.g. chemical shift and heteronuclear dipolar coupling frequencies) measured in separated local field [21] and other high-resolution solid-state NMR experiments. This information can be obtained not only for immobile systems but also in MAS studies of oriented samples [24,25]. The structures of gramicidin [26], the transmembrane M2 domain of the acetylcholine receptor [27], the transmembrane domain of the M2 protein from the influenza A virus [28], the membrane-bound form of coat protein [29], the transmembrane domain of Vpu [30], and the mercury transport membrane protein MerFt [31] have been obtained in bilayers mechanically aligned on glass plates or in magnetically aligned bicelles [32,33].

Further advances in structure determination of aligned membrane proteins by solid-state NMR require improved pulse sequences that will enable high resolution spectra to be obtained over the entire frequency span of the relevant spin interactions at high magnetic fields. This requirement arises not only from the increasing size and complexity of the proteins under investigation, but also the increasing use of high fields to improve sensitivity and chemical shift resolution. We are particularly concerned with the large dispersion of the amide ^1H chemical shift ranges (~13.5 kHz at 900 MHz compared to ~7.5 kHz at 500 MHz) in uniformly ^{15}N labeled proteins. The frequency-switched Lee–Goldburg (FSLG) scheme [5] constitutes one of the principal methods for obtaining high resolution separated local field experiments and is implemented in PISEMA [23]. Since this pulse sequence relies on off-resonant irradiation of the ^1H spins at theoretically calculated offset frequencies, it is sensitive to the frequency offsets resulting from large ^1H chemical shift dispersion found in proteins at high fields. This leads to variations of the scaling factor, line shape distortions, and loss of resolution for some of the signals in the spectrum. Recently, an improved PISEMA sequence has been demonstrated [34,35], which involves a refocusing 180° pulse to compensate for the proton chemical shift dispersion. It was shown to work in partially ordered dilute spin systems such as liquid crystals or under magic-angle spinning conditions. However, in strongly coupled oriented spin systems, such as membrane proteins in lipid bilayers, the finite 180° pulses interfere with the overall scaling factor resulting in incomplete averaging of the proton dipolar couplings and consequently loss of spectral resolution.

There is a need for more robust pulse sequences, which are less sensitive to the ^1H chemical shift dispersion at the moderate rf power levels that can be realistically applied to aqueous protein samples at high fields. In a recent communication [22], we described an initial version of such a pulse sequence, SAMMY, which works by averaging out the homonuclear spin–spin interactions using modified magic sandwiches [15,16]. SAMMY is less sensitive to the ^1H chemical shift dispersion than PISEMA and generally yields spectra with more uniform spectral linewidths and intensities over a relatively broad range of ^1H–^{15}N heteronuclear dipolar coupling and ^{15}N and ^1H chemical shift

frequencies. However, the linewidths for most resonances in the heteronuclear dipolar coupling dimension of two-dimensional SAMMY spectra are typically about 50% greater than the best linewidths obtained for some resonances by PISEMA. An obvious goal is to combine the broadband capability of SAMMY with the line-narrowing capability of PISEMA in a single experiment. The development of a pulse sequence designed for this purpose, as described in this Article, required a thorough analysis of the averaging of spin interactions by rf pulses. An improved version of SAMMY, which we call SAMPI4, yields linewidths similar to those of PISEMA (<200 Hz in the heteronuclear dipolar coupling frequency dimension) with the advantage of covering the broad ranges of frequencies encountered in aligned samples of proteins at high fields. The spin dynamics of FSLG and PISEMA have been described elsewhere [5,36,37]. Here, a detailed analysis of the spin Hamiltonians of SAMPI4 is presented and the scaling factor for this pulse sequence is derived. In addition, SAMPI4 can be used as a building block for other multidimensional solid-state NMR pulse sequences, and a SAMPI4-based heteronuclear correlation (HETCOR) is demonstrated, including on a uniformly ^{15}N labeled membrane protein in aligned bicelles.

2. Theory

The SAMPI4 pulse sequence diagrammed in Fig. 1 is a further evolution of the experimental methods used for obtaining high resolution separated local field spectra. On the one hand, SAMPI4 appears to be a relatively minor improvement on the original SAMMY sequence [22] in that there is only one phase alteration on the low (e.g. ^{15}N or ^{13}C) channel, which improves the performance by decreasing the number of phase transients. On the other hand, its development required consideration of the most fundamental aspects of the averaging of spin interactions discussed in Section 1. Thus, this pulse sequence provides an example of the integration of theoretical aspects of

NMR spectroscopy and the practical aspects of using solid-state NMR for structure determination of proteins.

In the timing diagram of SAMPI4 in Fig. 1, the phases of the even t_1 dwells are shifted 180° compared to those of the odd dwells. Such 180° phase cycling removes the ^{1}H chemical shift evolution, further reduces the number of phase transients, and greatly reduces the deleterious effects of using finite Y90 pulses in the middle of each dwell. Previously [22], we found semi-empirically that by slightly shortening the lengths of each of the three SAMMY subperiods narrower linewidths could be obtained in the dipolar coupling frequency dimension of the resulting spectra. For example, we found that $\delta_1 = 0$ and $\delta_2 = 2\,\mu s$ for a 4.2 μs duration 90° pulse gave very good results. Here, we demonstrate that a quantum-mechanical derivation for the general case yields the optimal values for the parameters δ_1 and δ_2.

The analysis of spin dynamics for composite-pulse sequences, such as SAMMY and SAMPI4, necessitates simplifications of the many-body Hamiltonians involved. First, we derive the SAMMY scaling factor under the assumptions of infinitely short Y90 pulses and $\delta_1 = \delta_2 = 0$. In the next subsection, we calculate the lengths of δ_1 and δ_2 that compensate for finite Y90 pulses. In subsequent derivations we consider only the right-hand side exponential propagators for each of the nth subperiod of the overall dwell. The exponential propagators are then used to calculate the free induction decay (FID) signal from the solution of the stationary density-matrix equation for the matrix ρ

$$\rho(\tau_{n2}) = e^{-iH_{n21}(\tau_{n2}-\tau_{n1})}\rho(\tau_{n1})e^{iH_{n21}(\tau_{n2}-\tau_{n1})}, \qquad (1)$$

where H_{n21} is the average Hamiltonian between the periods τ_{n1} and τ_{n2} in the pulse sequence. The FID signal in the rotating frame after the total time t is then calculated in the standard manner as

$$G(t) = \mathrm{Trace}[S_x\rho(t)]. \qquad (2)$$

In order to derive analytic solutions, we use the doubly tilted frame [38], in which

$$G(t) = \mathrm{Trace}[S_z Y_S Y_I \rho(t)\overline{Y}_S\overline{Y}_I]. \qquad (3)$$

Here Y_S and Y_I are the rotation operators corresponding to a 90° rotation about the Y-axis applied to either the S spin or all I spins at the same time, and a bar denotes inverse rotation.

2.1. Derivation of the scaling factor in the limit of δ-pulse approximation

We derive the scaling factor for the simplified pulse sequence shown in Fig. 2 in the limit of the δ-pulse approximation for the Y90 pulses in the middle of single SAMMY t_1 dwell and no phase cycling. We also assume that both the low spin S and the high spins I are on resonance and the amplitudes of their radiofrequency fields exactly match the Hartmann–Hahn condition [39]. The interaction
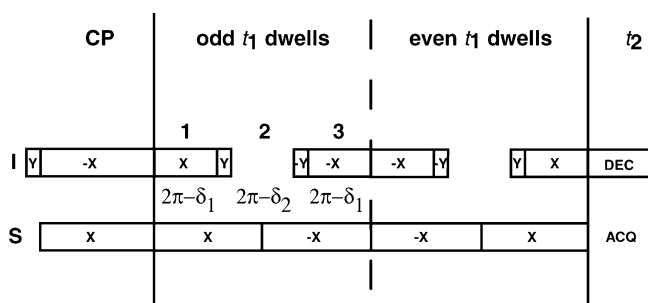

Fig. 1. Timing diagram for the SAMPI4 pulse sequence. Only one phase alteration on the low side is used, which decreases the number of phase transients. The length of each interval corresponds to the durations of the rf pulses as shown. The phases of the even t_1 dwells are 180° phase shifted compared to that of the odd dwell. To compensate for the finite Y90 pulses in the middle of each dwell, δ_1 and δ_2 are chosen as: $\delta_1 = \pi/(4\omega_1)$, $\delta_2 = \pi/(2\omega_1)$.
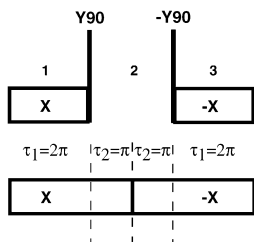
Fig. 2. Timing diagram for the SAMMY pulse sequence, [22] in the δ-pulse approximation. The length of each interval corresponds to the durations of the rf pulses as shown.

Hamiltonian describing the heteronuclear couplings between the S spin (e.g. ^{15}N or ^{13}C) and the I spins (i.e. ^{1}H) is defined as

$$H^{(IS)} = \sum_{i=1}^{N} a_i S_z I_z^{(i)}, \tag{4}$$

and the homonuclear couplings among the I spins are given by

$$H_{zz} = \sum_{i<j}^{N} \frac{b_{ij}}{2} [3 I_z^{(i)} I_z^{(j)} - (\mathbf{I}^{(i)} \mathbf{I}^{(j)})]. \tag{5}$$

For the first subperiod of the SAMMY cycle when all spins are irradiated the overall Hamiltonian is transformed as

$$\omega_1 (S_x + I_x) + H^{(IS)} + H_{zz} \approx Y_S Y_I [-\omega_1 (S_z + I_z) \\ + H_{\pm} - \tfrac{1}{2} H_{zz}] \overline{Y}_S \overline{Y}_I. \tag{6}$$

Only those terms that commute with the dominant radiofrequency irradiation term $\omega_1 (S_z + I_z)$ are retained whereas the higher order terms are left out by truncation. Therefore, the leading term for the heteronuclear interaction consists of only the spin flip-flop terms

$$H_{\pm} = \sum_{i=1}^{N} \frac{a_i}{4} [S_+ I_-^{(i)} + S_- I_+^{(i)}]. \tag{7}$$

We assume that the heteronuclear evolution is governed by the largest coupling $a = a_{max}$ between spin S and the neighboring spin I. For the two-spin case there is no homonuclear interaction H_{zz} and, therefore, it can be omitted from the calculations until the next subsection. Choosing $\tau_1 = 2\pi/\omega_1$, the overall SAMMY dwell in the doubly tilted frame becomes

$$e^{i\tau_1 H_{\pm}} \overline{Y}_S e^{i\tau_2 (\omega_1 S_x + a S_z I_z)} e^{i\tau_2 (-\omega_1 S_x + a S_z I_z)} Y_S e^{i\tau_1 H_{\pm}}. \tag{8}$$

Using the transformation

$$e^{-i\theta S_z I_z} S_x e^{i\theta S_z I_z} = S_x \cos\frac{\theta}{2} + 2 S_y I_z \sin\frac{\theta}{2}, \tag{9}$$

where $\tan(\theta/2) = a_{max}/(2\omega_1)$, the dwell propagator is expanded as

$$e^{i\tau_1 H_{\pm}} \overline{Y}_S \overline{X}_S e^{-i\theta S_z I_z} e^{i\tau_2 \sqrt{\omega_1^2 + a_{max}^2/4} S_x} e^{2i\theta S_z I_z} e^{-i\tau_2 \sqrt{\omega_1^2 + a_{max}^2/4} S_x} \\ \times e^{-i\theta S_z I_z} X_S Y_S e^{i\tau_1 H_{\pm}}. \tag{10}$$

Here the 90° rotation operator $X_{S,I}$ (and subsequently $Z_{S,I}$ in the following subsection) is defined similarly to $Y_{S,I}$. To achieve cancellation of the homonuclear terms in the many-spin case, τ_2 must be chosen as $\tau_2 = \pi/\omega_1$. At sufficiently high levels of radiofrequency irradiation $\omega_1^2 \gg a_{max}^2/4$, and $\theta \approx a_{max}/\omega_1$, which simplifies the propagator to

$$e^{i\tau_1 H_{\pm}} e^{-4i\theta S_y I_z} e^{i\tau_1 H_{\pm}} \approx e^{2i\tau_1 (H_{\pm} - \frac{a_{max}}{\pi} S_y I_z) + O(\tau_1^3)}. \tag{11}$$

Due to the symmetric nature of the product of the exponentials, Eq. (11) represents a second-order symplectic integrator [40] and the system evolves under the sum of the Hamiltonians up to the third order in time. This approximation becomes increasingly valid as the times τ_1 and τ_2 become shorter (or, alternatively, when the applied radiofrequency power is increased). The Hamiltonian can be explicitly diagonalized in the two-body case, which yields the following eigenvalues:

$$\lambda = \pm \frac{\pi \pm \sqrt{\pi^2 + 4}}{2\pi} \frac{a_{max}}{2} \\ = \pm 1.0927 \frac{a_{max}}{2} \text{ or } \pm 0.0927 \frac{a_{max}}{2}. \tag{12}$$

This means that during the middle part of the SAMMY sequence additional evolution of the heteronuclear coupling takes place, which affects the observed dipolar couplings and adds an additional smaller doublet to the spectra. Fortunately, the second doublet is of low intensity, and nearly disappears in the many-body case. This is illustrated in Fig. 3. Fig. 3A shows the result of a two-body simulation of the "ideal" SAMMY spectrum (cf. Fig. 2) with a_{max} set to 10 kHz between a ^{1}H and a ^{15}N. Fig. 3B shows the corresponding result for a many-body simulation of a 12-spin system consisting of one ^{15}N, one directly bonded ^{1}H, and 10 distant ^{1}H for the pulse sequence of Fig. 1. The spatial coordinates for the nuclei are those of an ideal α-helix tilted at 30° relative to the direction of the applied magnetic field. In both cases, the matrix exponentials in Eqs. (1) and (2) are calculated by numerical diagonalization using a MATLAB (www.mathworks.com) script. In Fig. 3A, two doublets can be seen, the main doublet is at ±5450 Hz and the secondary one is at ±450 Hz. This is to be compared with the theoretically predicted values (from Eq. (12)) of ±5464 and ±464 Hz. In the 12-spin case (Fig. 3B) the main doublet is observed at ±5508 Hz. Therefore, the observable splitting in SAMMY is approximately 9% greater than the real coupling, which means that the apparent dwell ($2\tau_1 = 4\pi/\omega_1$) should be adjusted accordingly.

2.2. Compensation for finite Y90 pulses—SAMPI4

In practice, it is necessary to deal with finite Y90 pulses during which some homonuclear and heteronuclear
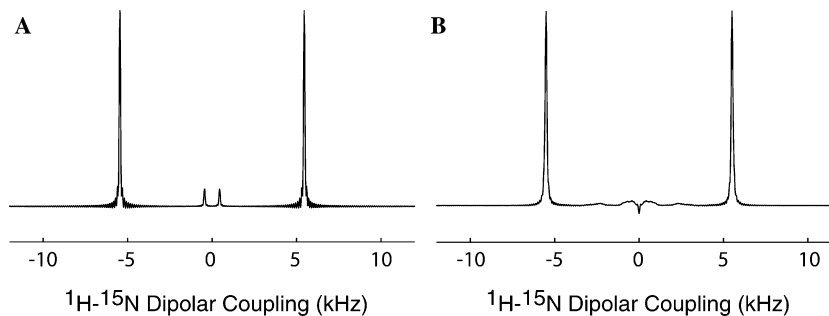
Fig. 3. Simulated spectra corresponding to the heteronuclear dipolar coupling frequency dimension of separated local field spectra. (A) Two-body simulation of idealized SAMMY. (B) Twelve-spin many-body simulation of SAMPI4. In both cases, a_{max} was set to 10 kHz and a 5 ms exponential decay function was applied to the calculated FID in the dipolar dimension. The magnitudes of the observed doublets are approximately 9% larger, which agrees with the scaling factor of Eq. (12). Note that the small doublet present in the middle of the spectrum disappears in the many-body case.

evolution can occur. Using the truncation principle of Eq. (6), during the finite Y90 pulse the Hamiltonians at sufficiently high rf power are transformed as

$$\omega_1(S_x + I_y) + H^{(IS)} + H_{zz}$$
$$\approx \overline{Z}_I Y_S Y_I \left[-\omega_1(S_z + I_z) + H_\pm - \tfrac{1}{2}H_{zz} \right] \overline{Y}_S \overline{Y}_I Z_I. \quad (13)$$

While higher-order terms may be significant in general, in the present case the magnetization in the tilted frame is mainly along the Z-axis, so the same truncation as in Eq. (6) is justified for Eq. (13) as well. For the duration of the 90-degree pulse, τ_{90}, the Y90 propagator of an odd dwell is written as:

$$Y_I X_S \overline{Z}_I Y_S Y_I \exp\left[i\tau_{90}\left(H_\pm - \tfrac{1}{2}H_{zz}\right) \right] \overline{Y}_S \overline{Y}_I Z_I$$
$$= Y_I Y_S \overline{Z}_S \overline{Z}_I Y_I \exp\left[i\tau_{90}\left(H_\pm - \tfrac{1}{2}H_{zz}\right) \right] \overline{Y}_S \overline{Y}_I Z_I$$
$$= Y_I Y_S \overline{X}_I \overline{Z}_S \overline{Z}_I \exp\left[i\tau_{90}\left(H_\pm - \tfrac{1}{2}H_{zz}\right) \right] Z_S \overline{Z}_S \overline{Y}_S Z_I X_I$$
$$= Y_I Y_S \overline{X}_I \exp\left[i\tau_{90}\left(H_\pm - \tfrac{1}{2}H_{zz}\right) \right] X_I \overline{Z}_S \overline{Y}_S. \quad (14)$$

(Since the effective Hamiltonian, $H_\pm - 1/2H_{zz}$ does not evolve under the $Z_S Z_I$ transformation.) Similarly, the $-$Y90 propagator is written as:

$$\overline{Z}_I Y_S Y_I \exp\left[i\tau_{90}\left(H_\pm - \tfrac{1}{2}H_{zz}\right) \right] \overline{Y}_S \overline{Y}_I Z_I \overline{Y}_I \overline{X}_S$$
$$= Y_S Z_S \overline{X}_I \exp\left[i\tau_{90}\left(H_\pm - \tfrac{1}{2}H_{zz}\right) \right] X_I \overline{Y}_S \overline{Y}_I. \quad (15)$$

For the even dwell Y90 propagator:

$$\overline{Y}_I \overline{X}_S \overline{Z}_I Y_S Y_I \exp\left[i\tau_{90}\left(H_\pm - \tfrac{1}{2}H_{zz}\right) \right] \overline{Y}_S \overline{Y}_I Z_I$$
$$= \overline{Y}_I Y_S Z_S \overline{Z}_I Y_I \exp\left[i\tau_{90}\left(H_\pm - \tfrac{1}{2}H_{zz}\right) \right] \overline{Y}_S \overline{Y}_I Z_I$$
$$= \overline{Y}_I Y_S \overline{X}_I Z_S \overline{Z}_I \exp\left[i\tau_{90}\left(H_\pm - \tfrac{1}{2}H_{zz}\right) \right] Z_I \overline{Z}_S Z_S \overline{Y}_S X_I$$
$$= \overline{Y}_I Y_S \overline{X}_I \exp\left[i\tau_{90}\left(-H_\pm - \tfrac{1}{2}H_{zz}\right) \right] X_I Z_S \overline{Y}_S, \quad (16)$$

and similarly for the $-$Y90 propagator of an even dwell:

$$\overline{Z}_I Y_S Y_I \exp\left[i\tau_{90}\left(H_\pm - \tfrac{1}{2}H_{zz}\right) \right] \overline{Y}_S \overline{Y}_I Z_I Y_I X_S$$
$$= Y_S \overline{Z}_S \overline{X}_I \exp\left[i\tau_{90}\left(-H_\pm - \tfrac{1}{2}H_{zz}\right) \right] X_I Y_I \overline{Y}_S. \quad (17)$$

For the purposes of this subsection, the small (about 9%) heteronuclear evolution during the middle part of SAM-MY can be neglected. Combining the first and last subperiods with the ±Y90 evolution and the middle part

(during which the system mainly evolves as H_{zz}) the overall odd-dwell propagator in the doubly tilted frame can be written as

$$e^{i\tau_1[-\omega_1(S_z+I_z)+H_\pm-\tfrac{1}{2}H_{zz}]} \overline{X}_I e^{i\tau_{90}(H_\pm-\tfrac{1}{2}H_{zz})} X_I e^{2i\tau_2 H_{zz}} \overline{X}_I e^{i\tau_{90}(H_\pm-\tfrac{1}{2}H_{zz})}$$
$$\times X_I e^{i\tau_1[\omega_1(S_z+I_z)+H_\pm-\tfrac{1}{2}H_{zz}]} \approx e^{i\tau_1[-\omega_1(S_z+I_z)+H_\pm-\tfrac{1}{2}H_{zz}]}$$
$$\times e^{i\tau_{90}(\tfrac{1}{2}H_\pm-\tfrac{1}{2}H_{yy})} e^{2i\tau_2 H_{zz}} e^{i\tau_{90}(\tfrac{1}{2}H_\pm-\tfrac{1}{2}H_{yy})} e^{i\tau_1[\omega_1(S_z+I_z)+H_\pm-\tfrac{1}{2}H_{zz}]}. \quad (18)$$

Only the zero-coherence heteronuclear terms have been retained, and the term H_{yy} is obtained from Eq. (5) by the substitution $z \rightarrow y$. For the even dwells

$$e^{i\tau_1[\omega_1(S_z+I_z)+H_\pm-\tfrac{1}{2}H_{zz}]} \overline{Y}_I(180) \overline{X}_I e^{i\tau_{90}(-H_\pm-\tfrac{1}{2}H_{zz})} X_I e^{2i\tau_2 H_{zz}} \overline{X}_I$$
$$\times e^{i\tau_{90}(-H_\pm-\tfrac{1}{2}H_{zz})} X_I Y_I(180) e^{i\tau_1[-\omega_1(S_z+I_z)+H_\pm-\tfrac{1}{2}H_{zz}]}$$
$$\approx e^{i\tau_1[\omega_1(S_z+I_z)+H_\pm-\tfrac{1}{2}H_{zz}]} e^{i\tau_{90}(\tfrac{1}{2}H_\pm-\tfrac{1}{2}H_{yy})} e^{2i\tau_2 H_{zz}} e^{i\tau_{90}(\tfrac{1}{2}H_\pm-\tfrac{1}{2}H_{yy})}$$
$$\times e^{i\tau_1[-\omega_1(S_z+I_z)+H_\pm-\tfrac{1}{2}H_{zz}]}. \quad (19)$$

As can be seen from Eq. (19), the 180° phase cycling is highly beneficial because it results in a 180-degree rotation about the Y-axis in the middle part of the pulse sequence, denoted by $Y_I(180)$, which refocuses any chemical shift evolution that may occur when the ^{1}H are not irradiated. For $\tau_1 = (2\pi - \pi/4)/\omega_1$, the combination of the odd and even dwells yields an extra $Z_S Z_I$ transformation, which results in the following effective odd-dwell propagator

$$e^{i\tau_1(H_\pm-\tfrac{1}{2}H_{zz})} e^{i\tau_{90}(\tfrac{1}{2}H_\pm-\tfrac{1}{2}H_{yy})} e^{2i\tau_2 H_{zz}} e^{i\tau_{90}(\tfrac{1}{2}H_\pm-\tfrac{1}{2}H_{yy})} e^{i\tau_1(H_\pm-\tfrac{1}{2}H_{zz})}. \quad (20)$$

And the effective even dwell becomes

$$e^{i\tau_1(H_\pm-\tfrac{1}{2}H_{zz})} e^{i\tau_{90}(\tfrac{1}{2}H_\pm-\tfrac{1}{2}H_{xx})} e^{2i\tau_2 H_{zz}} e^{i\tau_{90}(\tfrac{1}{2}H_\pm-\tfrac{1}{2}H_{xx})} e^{i\tau_1(H_\pm-\tfrac{1}{2}H_{zz})}. \quad (21)$$

Using the equality $H_{xx} + H_{yy} + H_{zz} = 0$, the even and odd dwells can be combined in a single simplified propagator, which describes the effect of the finite $\pm$Y90 pulses

$$e^{i\tau_1(H_\pm-\tfrac{1}{2}H_{zz})} e^{i\tau_{90}(\tfrac{1}{2}H_\pm+\tfrac{1}{4}H_{zz})} e^{2i\tau_2 H_{zz}} e^{i\tau_{90}(\tfrac{1}{2}H_\pm+\tfrac{1}{4}H_{zz})} e^{i\tau_1(H_\pm-\tfrac{1}{2}H_{zz})}. \quad (22)$$

The cancellation of the homonuclear terms occurs when $\tau_1 = (2\pi - \pi/4)/\omega_1 = 7\pi/(4\omega_1)$ and $\tau_2 = (\pi - \pi/4)/\omega_1 = 3\pi/(4\omega_1)$. Because the $\pi/4$-pulse lengths compensate for the finiteness of the 90Y-pulses we refer to the pulse sequence as SAMPI4. Note that in both SAMPI4 (Fig. 1) and the ideal SAMMY (Fig. 2), the heteronuclear interactions still sum up

to the apparent $4\pi/\omega_1$ dwell. This dwell must be corrected by the factor 1.093, as described in the previous Section due to incomplete heteronuclear decoupling when the protons are not irradiated.

2.3. Incorporation of SAMPI4 into heteronuclear spin-correlation (HETCOR) experiment

The broad bandwidth of SAMPI4 makes it a valuable building block for other pulse sequences, including the solid-state NMR ^{1}H–^{15}N HETCOR experiment [41], which correlates ^{1}H and ^{15}N chemical shift frequencies in two-dimensional spectra. The modified HETCOR sequence is shown in Fig. 4. The first part of this pulse sequence still consists of FSLG for ^{1}H chemical shift evolution in the presence of homonuclear decoupling. After the t_1 evolution period and the $X_I(90)$ pulse the density matrix is (under the conditions of complete decoupling and high rf power)

$$\rho(t_1) = I_z \cos\left(\frac{\sigma_H}{\sqrt{3}}t_1\right) - I_x \sin\left(\frac{\sigma_H}{\sqrt{3}}t_1\right), \tag{23}$$

where σ_H is the proton chemical shift scaled by FSLG by a factor of 0.58. SAMPI4 is used to achieve selective polari-
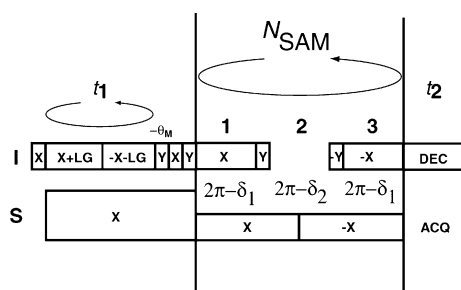
Fig. 4. Timing diagram for the HETCOR experiment incorporating SAMPI4 to achieve selective polarization transfer. During the t_1 period, the ^{1}H chemical shifts evolve under conditions of FSLG decoupling and high-power continuous rf irradiation of ^{15}N. The third intermittent Y90 pulse after the t_1 evolution pulse interleaves real and imaginary parts. The optimal number of SAMPI4 cycles is between 4 and 10 in this application.

zation transfer for the amide ^{1}H to the covalently bonded ^{15}N. The optimal number of SAMPI4 dwells N_{SAM} (with the appropriate 180-degree cycling as in Fig. 1) to achieve the transfer for all peaks depends on the orientation and is typically found to be between 4 and 10. To measure both the real and imaginary components of the ^{1}H chemical shift evolution, an intermediate $Y_I(90)$ pulse is used. If the polarization in the laboratory frame is along the Z-axis, it does not evolve under SAMPI4. Therefore, when present, the intermediate $Y_I(90)$ pulse selects the cosine term by placing the I_z term along the X-axis; when it is absent, only the sine term evolves.

3. Results and discussion

In order to work with spectra containing relatively few resonances spread over a broad range of frequencies we used a "multicrystal" sample consisting of three small crystals of ^{15}N-acetyl-leucine, each at an arbitrary orientation. Fig. 5A is a SAMPI4 spectrum obtained with rf power corresponding to a 4.4 µs 90° pulse (56.8 kHz B_1 field strength). Since each single crystal has 4 amide sites at distinct orientations, a total of 12 signals are expected. The experimental spectrum contains 11 signals, with two overlapped resonances contributing to the signal near 110 ppm (as shown in subsequent PISEMA and HETCOR spectra). The signals are numbered 1–12 in descending order of their chemical shift frequencies. The contour line corresponds to the two-dimensional powder pattern defining the span of frequencies for the ^{1}H and ^{15}N interactions at the amide sites. The powder pattern was calculated by a Monte-Carlo simulation using consensus parameters (except Gly and Pro) for the ^{15}N chemical shift tensor ($\sigma_{11} = 64$ ppm, $\sigma_{22} = 77$ ppm, $\sigma_{33} = 220$ ppm, $\beta = 18.0°$) and $r_{NH} = 1.05$ Å. A representative slice through the indirect dimension is shown. A notable feature of spectra obtained with SAMPI4 is a significant reduction in the amplitude of the zero-frequency artifact, which is often observed in PISEMA spectra.
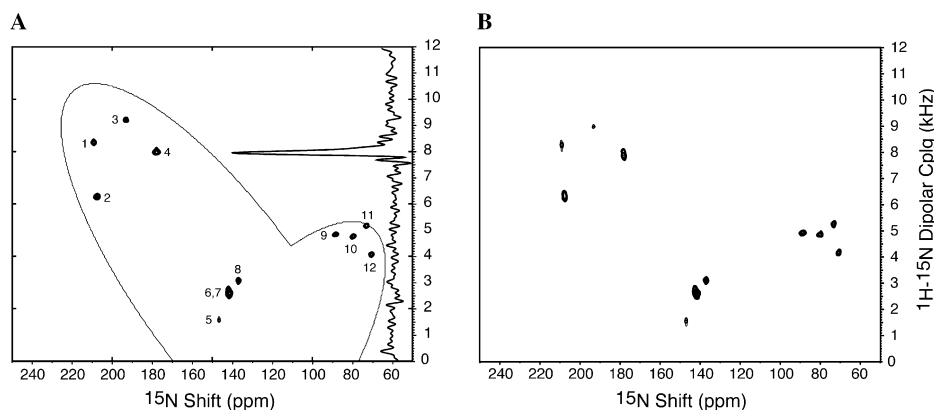

Fig. 5. Comparison of SAMPI4 and SAMMY of a multicrystal sample consisting of three single crystals of NAL at arbitrary orientations. (A) SAMPI4 spectrum. The contour line corresponds to the two-dimensional powder pattern calculated using the average ^{15}N CSA tensor parameters: $\sigma_{11} = 64$ ppm, $\sigma_{22} = 77$ ppm, $\sigma_{33} = 220$ ppm, $\beta = 18.0°$, and $r_{NH} = 1.05$ Å. Lorentzian linewidths for the peaks numbered 1–12 are: (1) 192 Hz; (2) 166 Hz; (3) 188 Hz; (4) 162 Hz; (5) 251 Hz; (6) and (7) 237 Hz; (8) 191 Hz; (9) 161 Hz; (10) 187 Hz; (11) 183 Hz; (12) 176 Hz. (B) SAMMY spectrum. Linewidths for peaks 1–12 are: (1) 228 Hz; (2) 315 Hz; (3) 256 Hz; (4) 350 Hz; (5) 234 Hz; (6) and (7) 204 Hz; (8) 193 Hz; (9) 165 Hz; (10) 185 Hz; (11) 184 Hz; (12) 202 Hz.

Fig. 5B is a SAMMY spectrum, obtained with the same power levels and carrier frequencies, using the original version of the pulse sequence [22]; it is apparent that the resonances with large heteronuclear dipolar couplings frequencies (>6 kHz) are much better decoupled using SAMPI4 than SAMMY. The SAMPI4 spectrum has linewidths of <200 Hz for almost all resonances.

The performance of SAMPI4 depends on the amount of rf power that is applied. Larger couplings (>5 kHz) are more affected by inadequate rf power levels. For example, for data acquired with a 50 kHz B_1 field strength (5 µs 90°

pulse, results not shown), the decoupling efficiency for peak #3 (9.2 kHz coupling) is significantly deteriorated, whereas peaks 8–12 still have linewidths <200 Hz. Fig. 6A contains PISEMA spectra obtained under exactly the same conditions as in Fig. 5; even though some of the linewidths are narrower than those obtained using SAMPI4 (130 Hz vs. 160 Hz in the best cases) more than half of the peaks did not evolve or decouple properly in the dipolar coupling frequency dimension. This situation can be remedied to a certain extent by shifting the ^{1}H carrier frequency several kHz during the t_1 evolution period. As an example,
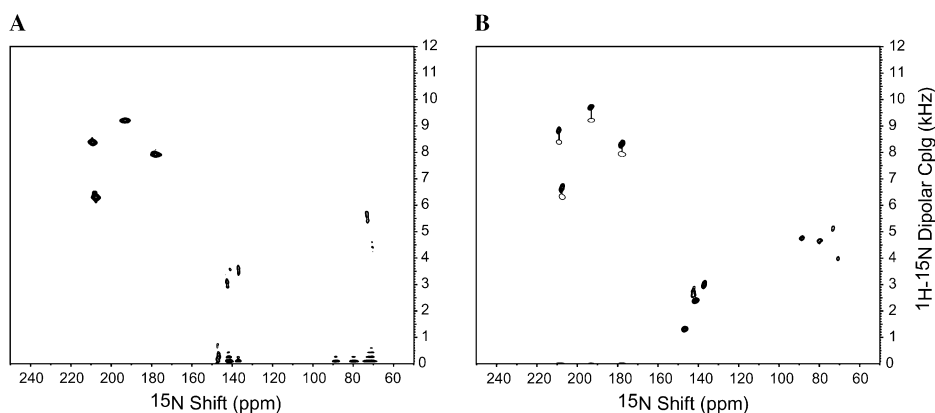

Fig. 6. Comparison of PISEMA spectra obtained with two different ^{1}H carrier frequencies. (A) At the optimal decoupling carrier determined by the t_2 evolution. Linewidths for peaks 1–4 are: (1) 149 Hz; (2) 149 Hz; (3) 130 Hz; (4) 130 Hz; whereas the remaining peaks did not properly evolve. (B) At ^{1}H carrier shifted up by 4 kHz during t_1 acquisition. Linewidths for peaks 1–12 are: (1) 212 Hz; (2) 211 Hz; (3) 182 Hz; (4) 170 Hz; (5) 149 Hz; (6) 240 Hz; (7) 141 Hz; (8) 205 Hz; (9) 176 Hz; (10) 195 Hz; (11) 253 Hz; (12) 228 Hz.
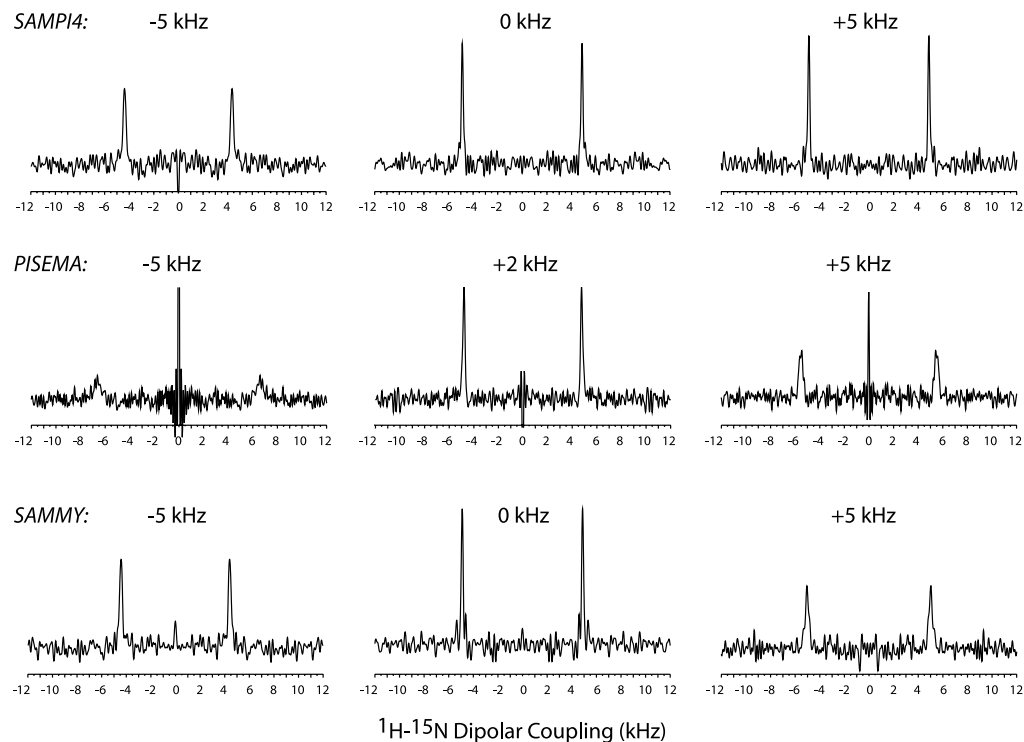

Fig. 7. Representative slices through the dipolar dimension for peak #9 at 500 MHz at different ^{1}H carrier offsets. First row: SAMPI4; second row: PISEMA; third row: SAMMY. SAMPI4 shows good decoupling over the entire range rf frequencies studied (±5 kHz). Note that for PISEMA the optimal decoupling condition is shifted by +2 kHz relative to SAMPI4/SAMMY for this peak.

Fig. 6B contains a PISEMA spectrum obtained under conditions where the ^{1}H central carrier frequency was shifted by 4 kHz during the FSLG irradiation interval. Because the line widths are relatively narrow, this appears to improve the broadband decoupling efficiency of PISEMA, however, the signals with larger dipolar couplings actually change their frequencies by as much as 600 Hz as a result of the offset dependence of the scaling factor. In the case of a protein, the resulting inaccuracies in the dipolar coupling frequencies would make them unsuitable as input for structure calculations. Note that due to the greater sensitivity of FSLG to ^{1}H frequency offsets, the broad intensity at 140 ppm becomes split into two peaks, which is due to the different chemical shifts of the directly bonded protons (see below).

Representative slices through the (indirect) heteronuclear dipolar coupling frequency dimension are shown in Fig. 7 for peak #9, which corresponds roughly to the perpendicular orientation of the N—H bond. For this orientation, PISEMA turns out to be the most sensitive to the ^{1}H carrier offset. By contrast, SAMPI4 turns out to be relatively insensitive to the positive offset and more sensitive to the negative offset. Notably, for this peak the optimal decoupling conditions for PISEMA differ by about 2 kHz from those for SAMPI4 of SAMMY.

The dependence of the scaling factor, as represented by the measured dipolar couplings, as a function of ^{1}H carrier

frequency is shown in the plots in Fig. 8 for SAMPI4 (solid line) and PISEMA (dashed line). In the case of aligned protein samples, care must be taken to determine the ^{1}H carrier frequency that provides optimal decoupling for the observed signals. In practice, this often means obtaining multiple spectra at different carrier frequencies.

It has been shown previously [22,35,37] that for PISEMA the optimal decoupling corresponds to the lowest point of the scaling factor "smile" for each peak. In this case the measured dipolar coupling corresponds to the actual N–H coupling. However, as can be seen from Fig. 8 this can be difficult to achieve simultaneously for all signals in a PISEMA spectrum. This is perhaps most pronounced for peaks #3 and #5, for which the difference in their optimal ^{1}H carrier frequency is 4 kHz. Moreover, if the frequency is optimized for one set of peaks, some peaks may not evolve at all. Interestingly, the likelihood of losing peaks entirely increases at lower carrier frequencies; at higher ^{1}H carrier frequencies most of the peaks do evolve during t_1. However, the dipolar scaling factor may become unreliable (cf. Fig. 6B). By contrast, SAMPI4 is much more tolerant of sub-optimal ^{1}H carrier offset frequencies, and gives almost flat profiles across a ±5 kHz range of ^{1}H offset frequencies. Moreover, all the peaks are evolved by SAMPI4 in the dipolar dimension regardless of the offset.

The magnitudes of the measured dipolar coupling frequencies for all eleven resolved resonances are plotted as
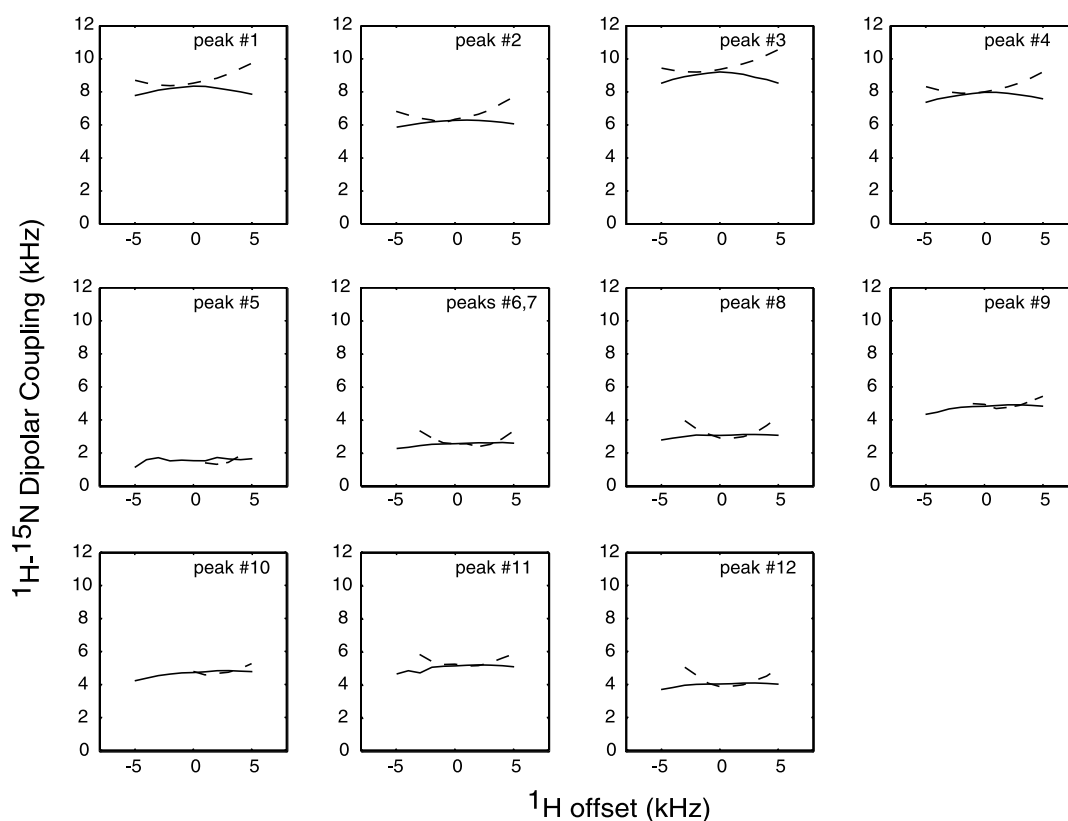

Fig. 8. Comparison of observed magnitudes of the heteronuclear dipolar couplings obtained using SAMPI4 (continuous lines) and PISEMA (dashed lines) as function of ^{1}H carrier offset for peaks 1–12.

a function of rf field strength in Fig. 9 for SAMPI4. The measurements were performed at 500 MHz using five different rf field strengths, corresponding to 90° pulse lengths: 3.7 μs (67.6 kHz B_1 field), 4.05 μs (61.7 kHz B_1 field), 4.45 μs (56.2 kHz B_1 field), 4.75 μs (52.6 kHz B_1 field), and 5.05 μs (49.5 kHz B_1 field). The scaling factors for the larger couplings (>8 kHz) are less reliable when the 90° pulse lengths are longer than 4.5 μs; whereas smaller (<5 kHz) couplings are relatively insensitive to the B_1 field strength within the range studied.

HETCOR spectra provide valuable complementary information about the ^1H carrier offset dependencies, since they show the distribution of ^1H chemical shifts for the various ^{15}N sites. Fig. 10 is a HETCOR spectrum obtained using the pulse sequence in Fig. 4 on the same multicrystal sample at the same orientation. The ^1H carrier frequency

was at 3.2 ppm. At this orientation, four SAMPI4 dwells were sufficient to selectively transfer polarization for all peaks. While peaks #1 and #2 appear to have similar ^1H and ^{15}N chemical shifts, the other 10 peaks are clearly resolved. The contour line corresponds to a two-dimensional powder pattern correlating the ^1H and ^{15}N chemical shift frequencies using the average ^1H principal values of $\sigma_{11} = 3$ ppm, $\sigma_{22} = 8$ ppm, and $\sigma_{33} = 17$ ppm [42]. The large difference in the optimal ^1H carrier observed in Fig. 8 for peaks #3 and #5 is most likely due to a difference of more than 8 ppm between the chemical shifts of the directly bound protons for these sites, which is revealed by the HETCOR spectrum.

The potential to use SAMPI4 to effect broadband polarization transfer at high fields was demonstrated at 900 MHz. Fig. 11 contains both SAMPI4 and HETCOR spectra of the same multicrystal sample at 900 MHz; however, the orientations of the individual crystals could not be preserved while transferring the sample between probes and spectrometers, and this accounts for the differences in resonance frequencies compared to Figs. 5, 6, and 10.
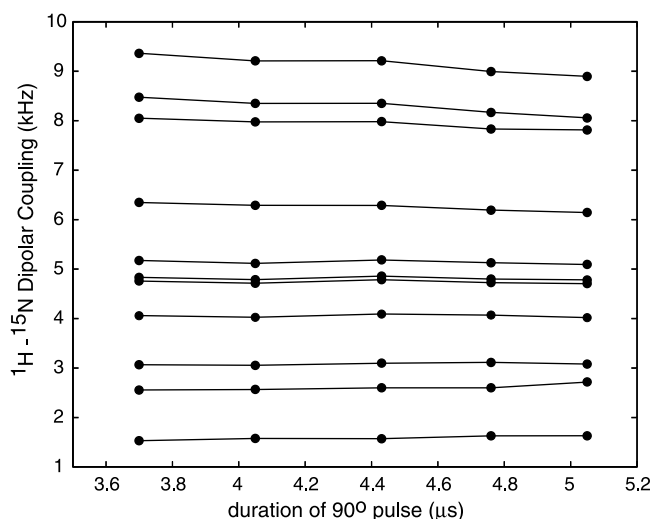

Fig. 9. The observed dipolar couplings for SAMPI4 as a function of applied rf power (length of the calibrated 90° pulse) for each resolved resonance at 500 MHz.
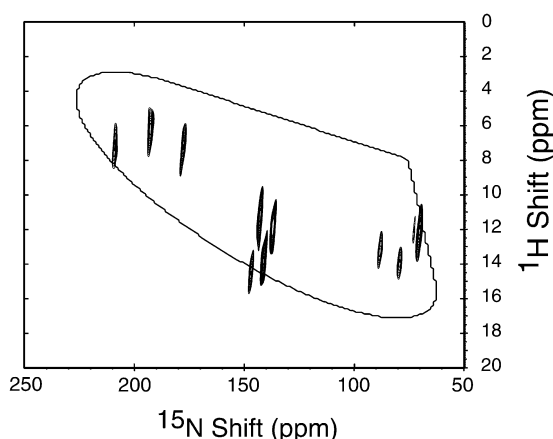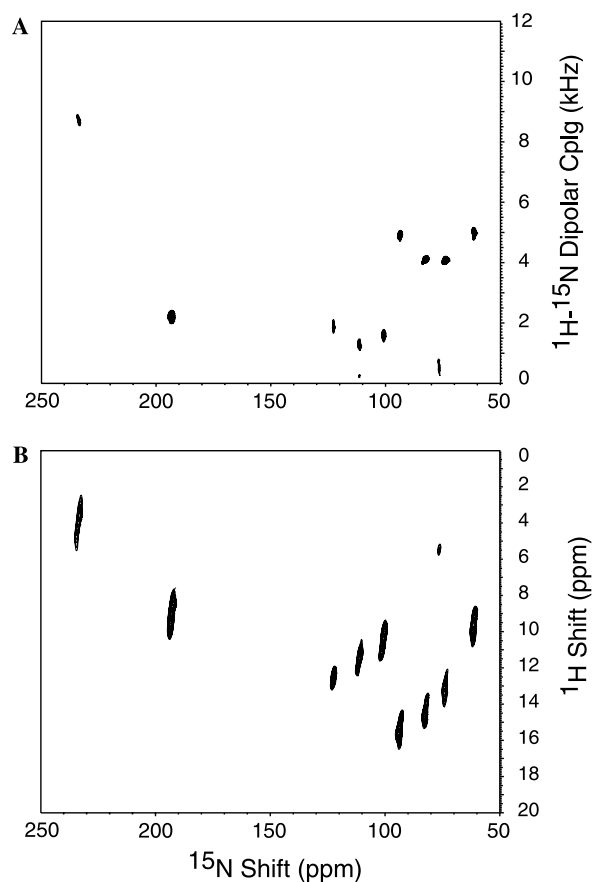

Fig. 10. HETCOR spectra obtained using SAMPI4 for selective transfer at 500 MHz. The ^1H carrier was set at 3.2 ppm. The observed range for ^1H chemical shifts is about 9 ppm or 4.5 kHz. The solid line denotes the boundary of the powder pattern covering the chemical shift range expected in proteins.

Fig. 11. Spectra of the multicrystal sample at 900 MHz at a different orientation. (A) SAMP14. (B) HETCOR. The 90° pulse was 4.2 μs. The ^1H carrier was set at 8.1 ppm. The observed range for ^1H chemical shifts is now 11.5 ppm or 10.4 kHz. At 900 MHz it is more difficult to achieve optimal decoupling in the dipolar dimension, especially for the larger couplings. However, effective polarization transfer can still be achieved by SAMPI4.

The 90° pulse was calibrated at 4.2 μs (60 kHz B_1 field strength). Compared to 500 MHz, even at higher B_1 field strengths, it is much more difficult at 900 MHz to find a single ^{1}H carrier frequency that yields <200 Hz linewidths for all signals. Furthermore, for this particular combination of crystal orientations, no single optimum number of SAMPI4 dwells was found that performed adequately for all resonances. The maximum number of peaks (10) that could be simultaneously observed via polarization transfer by 9 SAMPI4 dwells is shown in Fig. 11B. The linewidths are constant in Hz, therefore they are effectively improved from 1.8 ppm at 500 MHz to about 1 ppm at 900 MHz. Despite the wide range of ^{1}H chemical shift frequencies (11.5 ppm or 10.4 kHz), SAMPI4 provided selective polarization transfer from the proton to its directly bonded nitrogen, which enables ^{15}N detection.

High magnetic fields provide not only greater ^{1}H chemical shift dispersion but also improved sensitivity. Fig. 12 compares two-dimensional SAMPI4 and HETCOR spectra obtained on a sample containing 1 mg of a uniformly ^{15}N labeled 37-residue polypeptide (the transmembrane domain of Vpu) reconstituted in perpendicular (unflipped) bicelles [32]. The 90° pulse was calibrated at 5.3 μs and 128

scans in the direct dimension were acquired for each of 64 t_1 points. Since all of the dipolar couplings are reduced by ∼40% in perpendicular bicelles, the pulse sequences were effective at the lower B_1 fields available for aqueous protein samples at high fields. The SAMPI4 spectrum shown in Fig. 12A exhibits excellent resolution for at least 23 peaks. The contour of the amide powder pattern was calculated assuming a bicelle order parameter of 0.8 and fast uniaxial diffusion for the amide N–H sites in the bicelles [43]. Fig. 12B shows the corresponding HETCOR spectrum, which gives the distribution of ^{1}H chemical shifts of the protein.

4. Conclusions

The bandwidth limitations encountered in applications of PISEMA and SAMMY for two-dimensional separated local field spectroscopy are reduced with SAMPI4, which is of crucial importance for studies of proteins in high magnetic fields. SAMPI4 can be readily implemented on commercial spectrometers since it does not involve frequency jumps or complex phase modulations. A SAMPI4-based selective transfer can be used as a building block for other two-dimensional pulse sequences such as two-dimensional HETCOR as well as three-dimensional experiments. Interestingly, while the FSLG scheme turns out to be very sensitive to the ^{1}H chemical shift dispersion when used to measure the [1]H–[15]N dipolar couplings, we have found it to be noticeably more robust when used to measure the ^{1}H chemical shifts themselves at resonance frequencies as high as 900 MHz.

A detailed treatment of the spin dynamics of SAMPI4 and a derivation of the scaling factor for this pulse sequences is presented. Justification of the correction lengths, which compensate for the finiteness of the Y90-degree pulses, δ_1 and δ_2 is given using quantum-mechanical exponential propagators. The treatment of the effective Hamiltonians is build upon symmetrization of the products of exponential operators and truncation of higher-order terms during the continuous rf irradiation. This method becomes valid at high powers where the relevant time intervals become sufficiently short and, as a result, the higher-order terms arising from non-commuting operators can be neglected. These power limits are determined by the magnitudes of spin interactions present in the sample.

The method of treating the heteronuclear and homonuclear Hamiltonians under relatively high rf irradiation powers has the potential to allow facile development of new pulse sequences for high-resolution solid-state NMR by eliminating the need to compensate for the imperfections of the sequences originally created under the δ-pulse approximation. This will improve the feasibility of determining the structures of larger and more complex membrane proteins in their native phospholipid environments, and more generally enabling NMR studies to tackle a greater fraction of the proteins expressed from genomes by overcoming the limitations resulting from the slow
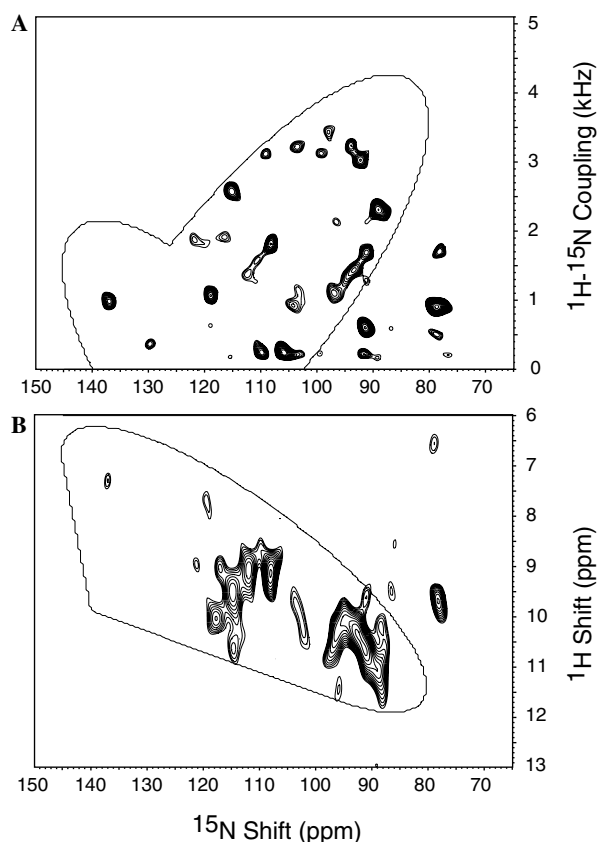

Fig. 12. Two-dimensional solid-state NMR spectra at 900 MHz of a uniformly ^{15}N labeled membrane protein in magnetically aligned bicelles. (A) SAMPI4. (B) HETCOR. The 90° pulse was calibrated at 5.3 μs. The contour lines show the powder patterns expected for amide resonances in perpendicular bicelles including the bicelle order parameter of 0.8. The signals that fall outside the contour lines are from sidechain resonances.

reorientation rates of proteins in biological supramolecular assemblies.

5. Experimental section

The NMR experiments were performed on spectrometers with ^{1}H resonance frequencies of 500 and 900 MHz. The 500 MHz spectrometer was configured with a Varian (www.varianinc.com) Inova console and a wide-bore Magnex 500/89 magnet and room temperature shim coils. A home-built lumped-element probe with a 5 mm inner diameter solenoid coil double-tuned to the ^{1}H and ^{15}N frequencies was utilized. The 900 MHz spectrometer was configured with a Bruker (www.bruker.com) Avance console and a standard-bore Magnex 900/52 magnet. A home-built double-tuned probe with a 4 mm inner diameter solenoid coil and Magnex room temperature shim coils were utilized. The principal sample consisted of three small crystals of ^{15}N-acetyl-leucine (NAL) packed inside a single glass tube. The sample of the membrane protein Vpu2-30+ was prepared in bicelles as described elsewhere [30,32]. One hundred and twenty-eight t_1 and 512 t_2 points were acquired in separated local-field experiments (SAMPI4, SAMMY, PISEMA) and 64 t_1 and 512 t_2 points in the heteronuclear correlation experiments with an 8 s recycle delay. Due to hardware limitations, a phase-modulated Lee–Goldburg scheme [6] was used on the INOVA console instead of FSLG. The number of scans was 16 at 500 MHz and 8 at 900 MHz for the crystal sample and 128 for the protein sample. The B_1 rf field strength was 56.8 kHz at 500 MHz (5 mm solenoid coil) and 60 kHz at 900 MHz (4 mm solenoid coil) for the sample containing crystals of NAL and 47.2 kHz for the protein sample. The SPINAL pulse sequence [44] was used for decoupling during data acquisition at 900 MHz. In the HET-COR experiments the ^{15}N decoupling power was increased by 50–60% to avoid the Hartmann–Hahn matching condition during ^{1}H chemical shift evolution. The NMR data were processed using nmrPipe [45] with 1 ppm Lorentzian line broadening in the direct dimension followed by Fourier transformation. No apodization function was applied in the indirect dimension on the crystal sample.

Acknowledgments

References

[1] E.R. Andrew, A. Bradbury, R.G. Eades, Removal of dipolar broadening of nuclear magnetic resonance spectra of solids by specimen rotation, Nature 183 (1959) 1802–1803.

[2] I.J. Lowe, Free induction decays of rotating solids, Phys. Rev. Lett. 2 (1959) 285–287.

[3] J. Schaefer, E.O. Stejskal, High-resolution ^{13}C NMR of solid polymers, in: G.C. Levy (Ed.), vol. 3, John Wiley & Sons, New York, 1979, pp. 283–324.

[4] M. Lee, W.I. Goldburg, Nuclear-magnetic-resonance line narrowing by a rotating Rf field, Phys. Rev. 140 (1965) 1261–1271.

[5] A. Bielecki, A.C. Kolbert, H.J.M. de Groot, R.G. Griffin, M.H. Levitt, Frequency-switched Lee–Goldburg sequences in solids, Adv. Magn. Reson. 14 (1990) 111.

[6] E. Vinogradov, P.K. Madhu, S. Vega, High-resolution proton solid-state NMR spectroscopy by phase-modulated Lee–Goldburg experiment, Chem. Phys. Lett. 314 (1999) 443–450.

[7] J.S. Waugh, L.M. Huber, U. Haeberlen, Approach to high-resolution NMR in solids, Phys. Rev. Lett. 20 (1968) 180–182.

[8] W.K. Rhim, D.D. Elleman, R.W. Vaughan, Analysis of multiple pulse NMR in solids, J. Chem. Phys. 59 (1973) 3740–3749.

[9] D.P. Burum, W.-K. Rhim, Analysis of multiple pulse NMR in solids. III, J. Chem. Phys. 71 (1979) 944–956.

[10] D.P. Burum, M. Linder, R.R. Ernst, Low-power multipulse line narrowing in solid-state NMR, J. Magn. Reson. 44 (1981) 173–188.

[11] S.V. Dvinskikh, K. Yamamoto, A. Ramamoorthy, Heteronuclear isotopic mixing separated local field NMR spectroscopy, J. Chem. Phys. 125 (2006) 034507.

[12] S.V. Dvinskikh, K. Yamamoto, A. Ramamoorthy, Separated local field NMR spectroscopy by windowless isotropic mixing, Chem. Phys. Lett. 419 (2006) 168–173.

[13] K. Yamamoto, S.V. Dvinskikh, A. Ramamoorthy, Measurement of heteronuclear dipolar couplings using a rotating frame solid state NMR experiment, Chem. Phys. Lett. 419 (2006) 533–536.

[14] M. Hohwy, C.P. Jaroniec, B. Reif, C.M. Rienstra, R.G. Griffin, Local structure and relaxation in solid-state NMR: accurate measurement of amide N–H bond lengths and H–N–H bond angles, J. Am. Chem. Soc. 122 (2000) 3218–3219.

[15] W.-K. Rhim, A. Pines, J.S. Waugh, Time-reversal experiments in dipolar-coupled spin systems, Phys. Rev. B 3 (1971) 684–696.

[16] K. Takegoshi, C.A. McDowell, A "Magic Echo" pulse sequence for the high-resolution NMR spectra of abundant spins in solids, Chem. Phys. Lett. 116 (1985) 100–104.

[17] M. Hohwy, N.C. Nielsen, Elimination of high order terms in multiple pulse nuclear magnetic resonance spectroscopy: application to homonuclear decoupling in solids, J. Chem. Phys. 106 (1997) 7571–7586.

[18] M.H. Levitt, Symmetry-based pulse sequences in magic-angle spinning solid-state NMR, in: D.M. Grant, R.K. Harris (Eds.), Encyclopedia of NMR, Wiley, Chichester, 2002, pp. 165–196.

[19] U. Haeberlen, J.S. Waugh, Coherent averaging effects in magnetic resonance, Phys. Rev. 175 (1968) 453–467.

[20] M. Mehring, Principles of High Resolution NMR in Solids, Springer-Verlag, Heidelberg, 1983.

[21] J.S. Waugh, Uncoupling of local field spectra in nuclear magnetic resonance—determination of atomic positions in solids, Proc. Natl. Acad. Sci. USA 73 (1976) 1394–1397.

[22] A.A. Nevzorov, S.J. Opella, A "Magic Sandwich" pulse sequence with reduced offset dependence for high-resolution separated local field spectroscopy, J. Magn. Reson. 164 (2003) 182–186.

[23] C.H. Wu, A. Ramamoorthy, S.J. Opella, High-resolution heteronuclear dipolar solid-state NMR spectroscopy, J. Magn. Reson. A 109 (1994) 270–272.

[24] C. Glaubitz, A. Watts, Magic angle-oriented sample spinning (MAOSS): a new approach toward biomembrane studies, J. Magn. Reson. 130 (1998) 305–316.

[25] B.J. Gross, J.M. Tanski, A.E. McDermott, Structure determination of aligned systems by solid-state NMR magic angle spinning methods, J. Magn. Reson. 176 (2005) 223–233.

[26] R.R. Ketchem, W. Hu, T.A. Cross, High-resolution conformation of gramicidin A in a lipid bilayer by solid-state NMR, Science 261 (1993) 1457–1460.

[27] S.J. Opella, F.M. Marassi, J.J. Gesell, A.P. Valente, Y. Kim, M. Oblatt-Montal, M. Montal, Structures of the M2 channel-lining segments from nicotinic acetylcholine and NMDA receptors by NMR spectroscopy, Nat. Struct. Biol. 6 (1999) 374–379.

[28] J. Wang, S. Kim, F. Kovacs, T.A. Cross, Structure of the transmembrane region of the M2 protein H+ channel, Protein Sci. 10 (2001) 2241–2250.

[29] F.M. Marassi, S.J. Opella, Simultaneous assignment and structure determination of a membrane protein from NMR orientational restraints, Protein Sci. 12 (2003) 403–411.

[30] S.H. Park, A.A. Mrse, A.A. Nevzorov, M.F. Mesleh, M. Oblatt-Montal, M. Montal, S.J. Opella, Three-dimensional structure of the channel-forming trans-membrane domain of virus protein "u" (Vpu) from HIV-1, J. Mol. Biol. 333 (2003) 409–424.

[31] A.A. DeAngelis, S.C. Howell, A.A. Nevzorov, S.J. Opella, Structure determination of a membrane protein with two trans-membrane helices in aligned phospholipid bicelles by solid-state NMR spectroscopy, J. Am. Chem. Soc. 128 (2006) 12256–12267.

[32] A.A. DeAngelis, A.A. Nevzorov, S.H. Park, S.C. Howell, A.A. Mrse, S.J. Opella, High-resolution NMR spectroscopy of membrane proteins in "unflipped" bicelles, J. Am. Chem. Soc. 126 (2004) 15340–15341.

[33] S.H. Park, S.J. Opella, Tilt angle of a trans-membrane helix is determined by hydrophobic mismatch, J. Mol. Biol. 350 (2005) 310–318.

[34] S.V. Dvinskikh, D. Sandström, Frequency offset refocused PISEMA-type sequences, J. Magn. Reson. 175 (2005) 163–169.

[35] K. Yamamoto, D.K. Lee, A. Ramamoorthy, Broadband-PISEMA solid-state NMR spectroscopy, Chem. Phys. Lett. 407 (2005) 289–293.

[36] M. Ravikumar, A. Ramamoorthy, Exact evaluation of the line narrowing effect of the Lee–Goldburg pulse sequence in solid state NMR spectroscopy, Chem. Phys. Lett. 286 (1998) 199–204.

[37] Z. Gan, Spin dynamics of polarization inversion spin exchange at the magic angle in multiple spin systems, J. Magn. Reson. 143 (2000) 136–143.

[38] M. Levitt, Heteronuclear cross polarization in liquid-state nuclear magnetic resonance: mismatch compensation and relaxation behavior, J. Chem. Phys. 94 (1990) 30–38.

[39] S.R. Hartmann, E.L. Hahn, Nuclear double resonance in the rotating frame, Phys. Rev. 128 (1962) 2042.

[40] H. Yoshida, Construction of higher-order symplectic integrators, Phys. Lett. A 150 (1990) 262–268.

[41] A. Ramamoorthy, C.H. Wu, S.J. Opella, Experimental aspects of multidimensional solid-state NMR correlation spectroscopy, J. Magn. Reson. 140 (1999) 131–140.

[42] C.H. Wu, A. Ramamoorthy, L.M. Gierash, S.J. Opella, Simultaneous characterization of the amide ^1H chemical shift, ^1H–^{15}N dipolar, and ^{15}N chemical shift interaction tensors in a peptide bond by three-dimensional solid-state NMR spectroscopy, J. Am. Chem. Soc. 117 (1995) 6148–6149.

[43] A.A. Nevzorov, A.A. DeAngelis, S.H. Park, S.J. Opella, Uniaxial motional averaging of the chemical shift anisotropy of membrane proteins in bilayer environments, in: A. Ramamoorthy (Ed.), NMR spectroscopy of Biological solids, Marcel Dekker, New York, 2005, pp. 177–190.

[44] B.M. Fung, A.K. Khitrin, K. Ermolaev, An improved broadband decoupling sequence for liquid crystals and solids, J. Magn. Reson. 142 (2000) 97–101.

[45] F. Delaglio, S. Grzesiek, G.W. Vuister, G. Zhu, J. Pfeifer, A. Bax, NMRPipe: a multidimensional spectral processing system based on UNIX pipes, J. Biomol. NMR 6 (1995) 277–293.